Physical explanation of the SLIPI technique by the large scatterer approximation of the RTE

Kristensson, Elias; Kristensson, Gerhard

2015

CODEN:LUTEDX/(TEAT-7238)/1-30/(2015)

Physical explanation of the SLIPI technique by the large scatterer approximation of the RTE

Elias Kristensson and Gerhard Kristensson

Electromagnetic Theory
Department of Electrical and Information Technology
Lund University
Sweden

(TEAT-7238)/1-30/(2015): E. Kristensson and G. Kristensson, Physical explanation of the SLIPI technique ...

Elias Kristensson
elias.kristensson@forbrf.lth.se

Department of Physics
Division of Combustion Physics
Lund University
P.O. Box 118
SE-221 00 Lund
Sweden

Gerhard Kristensson
Gerhard.Kristensson@eit.lth.se

Department of Electrical and Information Technology
Electromagnetic Theory
Lund University
P.O. Box 118
SE-221 00 Lund
Sweden

This is an author produced preprint version as part of a technical report series from the Electromagnetic Theory group at Lund University, Sweden. Homepage `http://www.eit.lth.se/teat`

Editor: Mats Gustafsson

Abstract

Visualizing the interior of a turbid scattering media by means light-based methods is not a straightforward task because of multiple light scattering, which generates image blur. To overcome this issue, a technique called Structured Laser Illumination Planar Imaging (SLIPI) was developed within the field of spray imaging. The method is based on a light coding strategy to distinguish between directly and multiply scattered light, allowing the intensity from the latter to be suppressed by means of data post-processing. Recently, the performance of the SLIPI technique was investigated, during which deviations from theoretical predictions were discovered. In this paper, we aim to better understand the origin of these deviations, and to achieve this end, we have performed several SLIPI measurements under well-controlled conditions. Our experimental results are compared with a theoretical model that is based on the large scatterer approximation of the Radiative Transfer Equation but modified according to certain constraints. Specifically, our model is designed to (1) ignore all off-axis intensity contributions and (2) to treat unperturbed- and forward-scattered light equally as we believe these to the rules governing the SLIPI technique. The comparison conclusively shows that optical measurements based on scattering and/or attenuation in turbid media can be subject to significant errors if not all aspects of light-matter interactions are considered. Our results indicate, as were expected, that forward-scattering can lead to deviations between experiments and theoretical predictions, especially when probing relatively large particles. However, rather unexpectedly, the model also suggests that the dimensions as well as the spreading of the light-probe are important factors one also needs to consider.

1 Introduction

Structured Laser Illumination Planar Imaging (SLIPI) is an optical imaging technique primarily used to visualize spray-related phenomena, such as the disintegration of liquid into fine, spherical droplets [1]. SLIPI is based on (1) laser sheet imaging [2], where a laser beam is formed into a thin sheet of light and (2) structured illumination [3], which employs an intensity modulation scheme to permit added post-processing possibilities. The purpose of a laser sheet is to illuminate only a single plane of the sample, *i.e.*, to optically select a "slice" of the sample. A camera positioned at a 90 degrees angle records the signal that is generated by the laser sheet, resulting in a 2D view of the illuminated sample.

The laser sheet technique has been widely used in several fields, such as combustion research, biology and fluid dynamics [2, 4, 5]. However, when the method is applied to optically dense, highly scattering environments, the electromagnetic field interacts in a complex way with the entire medium — not only with the droplets in the laser sheet, but also with the ones outside. Multiple scattering effects dominates in this situation. As the laser sheet method assumes direct scattering only, the detection of multiply scattered light causes measurement errors such as a reduced image contrast, concealment of structures and incorrect intensity levels [6]. To address this issue, laser sheet imaging can be combined with the structured

illumination method — a unification named SLIPI. With SLIPI, the laser beam is guided through a transmission Ronchi grating, which adds a sinusoidal line structure to the otherwise homogeneous (top-hat like) intensity profile of the laser sheet. The line structure has one primary purpose: providing means to differentiate between light that has been repeatedly scattered within the sample and light that has only interacted with the sample once. Only light that is directly scattered from the laser sheet to the detector is guaranteed to preserve this superimposed line structure in the detected image, whereas light that has been scattered several times lose this structural information. By post-processing the acquired data, the latter unwanted contribution can be greatly suppressed, leading to improved visualization of turbid, scattering objects.

In an attempt to better understand the potential and limitations of the SLIPI technique Kristensson and coworkers performed measurements on several cuvettes with a homogeneous mixture of water and polystyrene spheres, which both scattered and absorbed light [7]. Number density and particle size were altered in a controlled fashion, allowed them to compare the results with the Bouguer-Beer law.[1] It was discovered that the SLIPI technique did not produce results in complete agreement with this well-known law. In particular, an increased particle size resulted in larger deviations from theoretical predictions, a trend that the authors attributed to differences in the scattering phase function of the particles. In the size-range 1 to 30 μm, larger particles have a pronounced forward scattering lobe that grows in magnitude with size. This implies that the light intensity is enhanced in the forward direction — the more the larger the particle. Since light that does not deviate from its initial trajectory will preserve the line structure employed in SLIPI, it cannot be suppressed with the technique, thus resulting in the observed deviations from the Bouguer-Beer law. Figure 1 illustrates this forward-scattering lobe structure for three particle sizes.

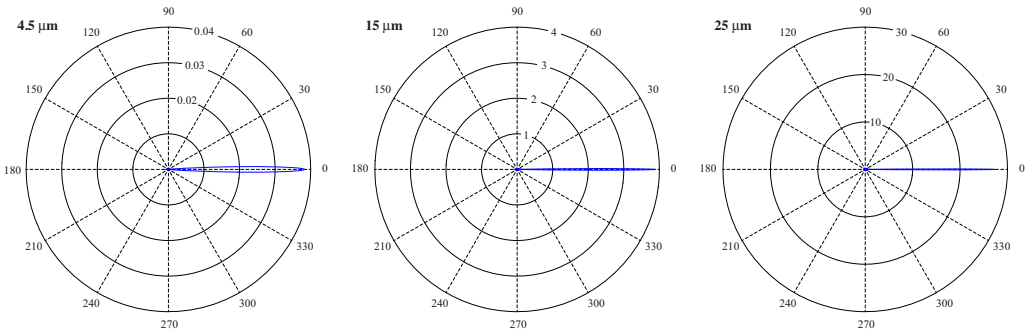

Figure 1: Mie scattering phase functions for three particle sizes ($\lambda = 447$ nm), shown in a *linear* scale. The (unconventional) linear representation of the scattering phase functions illustrates the strong forward-scattering phenomenon.

[1] Also known as Beer's law, the Beer-Lambert law, the Lambert-Beer law, or the Beer-Lambert-Bouguer law *etc.*, but it is incorrect to accredit Lambert to this law, since Bouguer made the original contributions [8]. For a comprehensive survey of the history of the law see [9].

This paper seeks to investigate the accuracy of this proposed explanation. To achieve this end and thereby better understand the physics governing light-matter interactions in general and the SLIPI technique in particular, we have performed SLIPI measurements under well-controlled conditions. The results are compared with theoretical prediction based on a solution of the Radiative Transfer Equation (RTE) using the large scatterer approximation.

2 Experimental arrangements

2.1 SLIPI optical setup

A schematic of the experimental setup is presented in Figure 2. The laser light ($\lambda = 447$ nm) was first expanded using a telescope of two lenses and then guided through an aperture to select the central, top-hat like region. The light was then guided through a Ronchi transmission grating, which diffracts the laser light, and a cylindrical lens focused the interference orders onto a so-called frequency cutter. The purpose of this device was to physically block all but the two fundamental orders. As these two identically intense beams overlapped they created, by interference, a sinusoidally modulated intensity profile. A second cylindrical lens was then used to focus the modulated light into a thin sheet of light (≈ 100 μm). A second telescope arrangement (cylindrical lenses) was used to alter the frequency of the intensity modulation. A sensitive EM-CCD (Andor Luca), mounted at a 90 degrees angle, was used to collect the signal from the laser sheet.

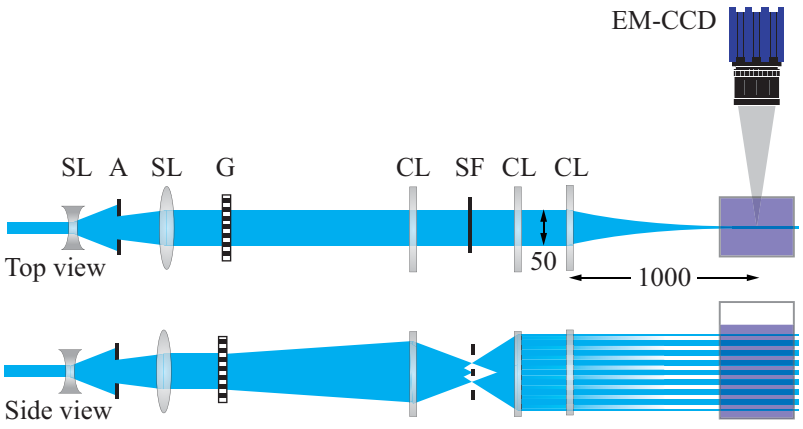

Figure 2: The experimental setup. SL = Spherical Lens. A = Aperture. G = Grating. CL = Cylinder Lens. SF = Spatial Filter.

The purpose of the modulation scheme is, as mentioned, to differentiate between the intensity contribution originating from singly- and multiply scattered light. Light that is repeatedly scattered within the sample tend to loose the modulation feature that is encoded into the illumination whereas directly (singly) scattered light remains faithful to this spatial structure. If the phase of the modulation structure

is slightly altered, the spatial distribution of the directly scattered light shifts accordingly, while the intensity contribution stemming from multiply scattered light remains unaffected. By calculating the pixel-wise root-mean-square (RMS) between three so-called subimages having spatial phases of 0, $2\pi/3$ and $4\pi/3$ the modulated component — the singly scattered light — is extracted and the DC-component — the multiply scattered light — is suppressed. An example of the process is given in Figure 3.

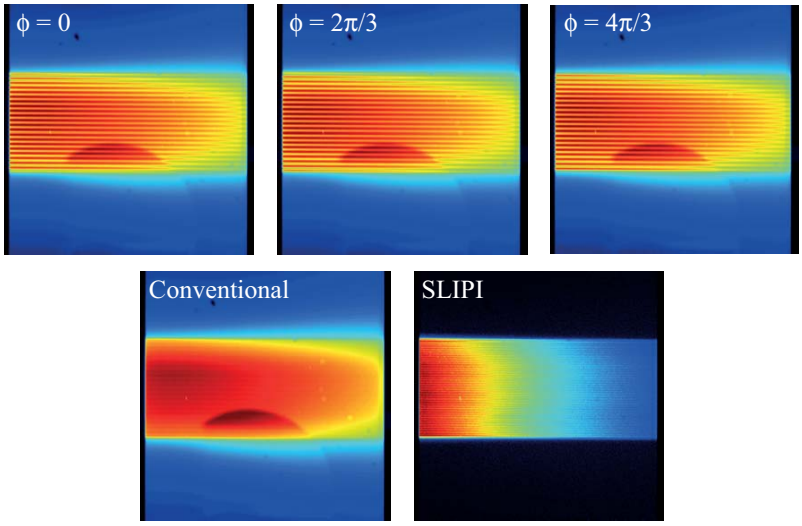

Figure 3: The SLIPI process, illustrated on one of the cuvettes used in the current study. To suppress the contribution from multiply scattered light (and other signal interferences), three so-called subimages are recorded, between which the spatial phase is altered 1/3 of the superimposed sinusoidal period. The "conventional" image shows the laser sheet signal without any suppression of the multiply scattered light, where unwanted signal stemming from non-irradiated regions of the sample can be observed. Such interferences are efficiently removed using the SLIPI data post-processing.

The SLIPI concept can be also understood in terms of spatial frequencies. All signal of interest is modulated by a well-defined spatial frequency while unwanted background features are characterized by other (not necessarily low) spatial frequencies. Calculating the pixel-wise RMS between the three subimages corresponds to extracting the image information modulated by the spatial frequency of the laser sheet.

2.2 Sample preparation

Six mixtures of water and non-absorbing microspheres were used in the experiments, having diameters of 4.5, 6, 10, 15, 20 and 25 μm, respectively. These particles were assumed to be spherical. All mixtures were prepared to have an opacity of $OD = 2$ (optical depth) over the distance 44 mm, corresponding to an average extinction of

0.045 mm^{-1}. The particles were delivered in 5 ml containers, with the total number of particles specified in each batch. By knowing the scattering cross-sections (σ_s) for the particles, the required number density corresponding to the desired average extinction could be calculated, see Table 1. Each sample was prepared according to the following procedure:

1. An empty 2 liters bottle was placed on a scale with milligram precision and its weight was noted.
2. The particles were emptied into to the bottle and the container carefully rinsed. The weight of the particles was neglected.
3. The amount of water specified in Table 1 was added to the bottle using the scale to monitor the added volume. Since the amount of water needed in each case differed, the precision of mixing process varied slightly.
4. 100 ml of the mixture was poured into a glass cuvette ($44 \times 34 \times 100$ mm^3).
5. To avoid particles sticking onto the glass surfaces, the cuvette was placed in an ultrasonic cleaner prior to the measurement.

Size [μm]	4.5	6	10	15	20	25
N	$2.495{\cdot}10^9$	$1.05{\cdot}10^9$	$2.275{\cdot}10^8$	$6.75{\cdot}10^8$	$2.84{\cdot}10^7$	$1.455{\cdot}10^7$
σ_s [μm^2]	35.0	60.9	208	407	571	984
H_2O [ml]	1986.46	1376.15	831.506	561.564	411.594	321.192
C [mm^{-3}]	1330	807	218	109	85.7	47.7

Table 1: Sample-related characteristics. N corresponds to the total number of particles in a 5 ml bottle, σ_s is the scattering cross-section, H_2O is the amount of water needed to achieve the desired concentration, C, that gives an OD of 2 over 44 mm. The explicit diameters delivered by the manufacturer were: 4.518, 5.94, 11.00, 15.66, 18.79, 24.90 μm, respectively.

2.3 Measurement scheme

Although the purpose of the investigation was to understand how differences in the Mie scattering phase function affected the outcome of a SLIPI measurement, direct comparison with the *scattered* light had to be avoided for experimental reasons. When visualizing the Mie scattered light from a spatially homogeneous sample with a polydisperse particle distribution, even minute changes in the collection- and acceptance angle will affect the resulting image because of the rapid angular variations in the Mie scattering phase function. Comparing the experimental data with the theoretical model would, in such a case, require the exact knowledge of the angle between laser sheet and the detector as well as the acceptance angles, which are

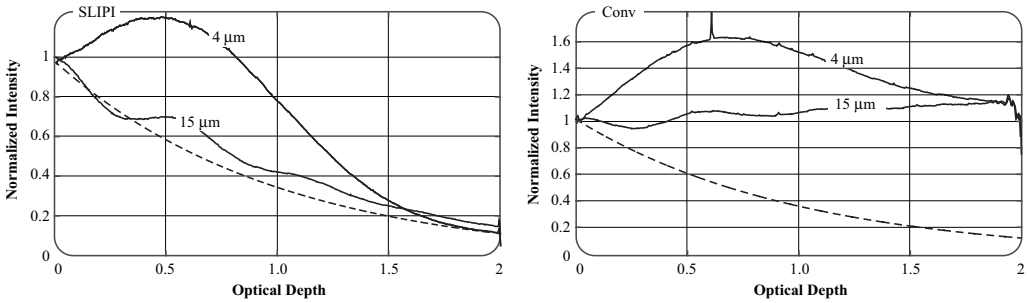

Figure 4: Cross-sections from two images where only elastically scattered light was collected, together with the decay of light intensity as predicted by the Bouguer-Beer law (dashed line). Both SLIPI and conventional data clearly show how the influence of the Mie scattering lobes make any theoretical comparisons challenging.

both difficult to assess with sufficiently high precision. Figure 4 shows Mie scattering images of the mixtures, where the influence of the lobe structures are noticeable.

To circumvent the issue with the side-scattering lobes experimentally, a small amount of fluorescing dye was added to each mixture. Since the in-elastic fluorescence signal is nearly isotopic and identical for all mixtures under study, the exact position of the camera with respect to the laser sheet is no longer a critical factor. By compensating for the loss of light introduced by the added dye ($OD \approx 0.1$), the approach thus allowed monitoring of the relative loss of photon energy as a function of distance, without being influenced by the specifics of the detection system. Figure 5 illustrates this procedure.

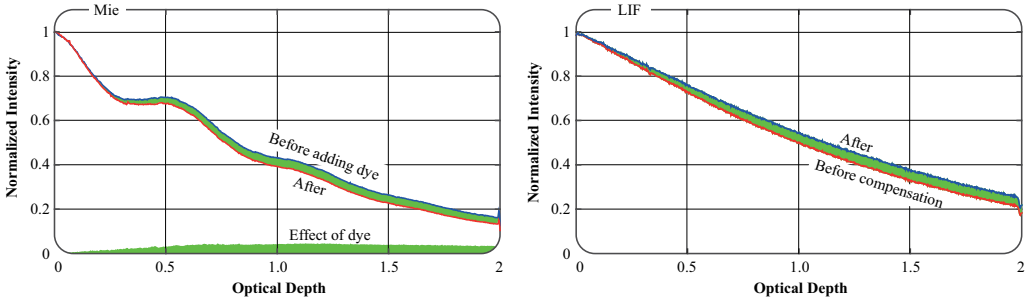

Figure 5: To avoid measurement uncertainties caused by the lobe structure of the scattering phase function, a small amount of fluorescing dye was added to the cuvette. SLIPI measurements were carried out both prior to and after the dye was added, thus permitting us to assess the slightly increased OD (left panel). As the dye emitted light nearly isotropically, the local light intensity *within* the cuvette could be monitored. However, since only the loss of energy caused by scattering was of interest, the added opacity of the dye was compensated for (right panel).

The refractive index of the spheres immersed in water is determined by [10]

$$n(\lambda) = A + \frac{B}{\lambda^2} + \frac{C}{\lambda^4}$$

where, if λ is the wavelength in vacuum measured in nm, the constants $A = 1.5725$, $B = 3108.0$, and $C = 34779 \cdot 10^4$.

3 Theory

The quantitative modeling of the SLIPI experiment is now addressed in detail. The aim of the theoretical model is to understand and explain the results of the SLIPI experiments, both qualitatively and quantitatively. To achieve this end, the model needs to accurately model the signal generated in a SLIPI measurement. The two main challenges of this task are: (1) the signal is generated by a laser *sheet* and (2) light contributions from other directions must be neglected (as these are suppressed with the SLIPI technique). Indeed, the theoretical model presented in this section corroborates all essential details of the experimental results and can, in fact, be used to design future experiments.

The radiative transfer equation (RTE) [11, 12] is commonly adopted as a model for computations of the intensity variations in random media. The RTE quantifies the intensity $I(\boldsymbol{r}, \hat{\boldsymbol{n}})$ at a point $\boldsymbol{r}$ in the medium in a specific direction $\hat{\boldsymbol{n}}$. The effect of the polarization state of the intensity is ignored in the scalar version of RTE. A vector formulation of RTE is available, which also quantifies the polarization effects by an employment of the Stokes parameters [13, 14]. However, the experimental results in this paper have very little polarization information, and, therefore, the scalar version of RTE suffices. Moreover, the RTE holds for sparse suspensions, which is assumed to hold for the suspensions used in this paper.

The RTE has no closed form solutions, and numerical techniques have to be employed. However, in several experimental situations approximations apply, which leads to closed form solutions of great value. One such approximation is the assumption of electrically large scatterer in the medium. In the results presented in this paper the scatterers are electrically large, $ka \approx [30, 165]$, where k is the wave number of the microspheres relative to the background material in the cuvette [10], and a is the average radius of the spheres. In this section, a review of the approximation employed in this paper is presented.

3.1 The radiative transport equation

The pertinent scalar version of the radiative transfer equation (RTE), or transport equation, for the intensity $I(\boldsymbol{r}, \hat{\boldsymbol{n}})$ at the position $\boldsymbol{r}$ in the direction $\hat{\boldsymbol{n}}$ is, see *e.g.*, [12, Ch. 7 & 11] or [13, Eq. (8.11.5)]

$$\hat{\boldsymbol{n}} \cdot \nabla I(\boldsymbol{r}, \hat{\boldsymbol{n}}) = -n_0(\boldsymbol{r}) \sigma_{\text{ext}}(\boldsymbol{r}, \hat{\boldsymbol{n}}) I(\boldsymbol{r}, \hat{\boldsymbol{n}}) + \frac{n_0(\boldsymbol{r})}{4\pi} \iint_{\Omega} \frac{\mathrm{d}\sigma}{\mathrm{d}\Omega}(\boldsymbol{r}, \hat{\boldsymbol{n}}, \hat{\boldsymbol{n}}') I(\boldsymbol{r}, \hat{\boldsymbol{n}}') \, \mathrm{d}\Omega'$$

where Ω denotes the unit sphere, $\mathrm{d}\Omega$ the surface measure on the unit sphere, $n_0(\boldsymbol{r})$ the number density (number of scatterers per unit volume) at $\boldsymbol{r}$, $\sigma_{\mathrm{ext}}(\boldsymbol{r}, \hat{\boldsymbol{n}})$ the extinction cross section at $\boldsymbol{r}$ (incident direction of the excitation is $\hat{\boldsymbol{n}}$), and where $\frac{\mathrm{d}\sigma}{\mathrm{d}\Omega}(\boldsymbol{r}, \hat{\boldsymbol{n}}, \hat{\boldsymbol{n}}')$ denotes the differential scattering cross section of the scatterer at $\boldsymbol{r}$ in the direction $\hat{\boldsymbol{n}}$ (incident direction $\hat{\boldsymbol{n}}'$). The scattering cross section $\sigma_{\mathrm{s}}(\boldsymbol{r}, \hat{\boldsymbol{n}}')$ is

$$\sigma_{\mathrm{s}}(\boldsymbol{r}, \hat{\boldsymbol{n}}') = \frac{1}{4\pi} \iint_{\Omega} \frac{\mathrm{d}\sigma}{\mathrm{d}\Omega}(\boldsymbol{r}, \hat{\boldsymbol{n}}, \hat{\boldsymbol{n}}') \, \mathrm{d}\Omega$$

Introduce the phase function $p(\boldsymbol{r}, \hat{\boldsymbol{n}}, \hat{\boldsymbol{n}}')$ defined as[2]

$$p(\boldsymbol{r}, \hat{\boldsymbol{n}}, \hat{\boldsymbol{n}}') = \frac{1}{4\pi\sigma_{\mathrm{ext}}(\boldsymbol{r}, \hat{\boldsymbol{n}}')} \frac{\mathrm{d}\sigma}{\mathrm{d}\Omega}(\boldsymbol{r}, \hat{\boldsymbol{n}}, \hat{\boldsymbol{n}}')$$

with normalization

$$\iint_{\Omega} p(\boldsymbol{r}, \hat{\boldsymbol{n}}, \hat{\boldsymbol{n}}') \, \mathrm{d}\Omega = \frac{\sigma_{\mathrm{s}}(\boldsymbol{r}, \hat{\boldsymbol{n}}')}{\sigma_{\mathrm{ext}}(\boldsymbol{r}, \hat{\boldsymbol{n}}')} = \alpha(\boldsymbol{r}, \hat{\boldsymbol{n}}')$$

where $\alpha(\boldsymbol{r}, \hat{\boldsymbol{n}}')$ denotes the single scatterer albedo. For spherical objects in a homogeneous material, the phase function depends only on the difference between the directions $\hat{\boldsymbol{n}}$ and $\hat{\boldsymbol{n}}'$ (more precisely the absolute value of the difference,[3] $|\hat{\boldsymbol{n}} - \hat{\boldsymbol{n}}'|$). The phase function for a homogeneous material of spherical scatterers then has the form

$$p(\hat{\boldsymbol{n}} - \hat{\boldsymbol{n}}') = \frac{1}{4\pi\sigma_{\mathrm{ext}}} \frac{\mathrm{d}\sigma}{\mathrm{d}\Omega}(\hat{\boldsymbol{n}} - \hat{\boldsymbol{n}}')$$

and the RTE simplifies to

$$\hat{\boldsymbol{n}} \cdot \nabla I(\boldsymbol{r}, \hat{\boldsymbol{n}}) = -n_0\sigma_{\mathrm{ext}} I(\boldsymbol{r}, \hat{\boldsymbol{n}}) + n_0\sigma_{\mathrm{ext}} \iint_{\Omega} p(\hat{\boldsymbol{n}} - \hat{\boldsymbol{n}}') I(\boldsymbol{r}, \hat{\boldsymbol{n}}') \, \mathrm{d}\Omega'$$

or if all distances are measured in units of the optical distance, OD (scale with $n_0\sigma_{\mathrm{ext}}$)

$$\hat{\boldsymbol{n}} \cdot \nabla_{\mathrm{OD}} I(\boldsymbol{r}_{\mathrm{OD}}, \hat{\boldsymbol{n}}) = -I(\boldsymbol{r}_{\mathrm{OD}}, \hat{\boldsymbol{n}}) + \iint_{\Omega} p(\hat{\boldsymbol{n}} - \hat{\boldsymbol{n}}') I(\boldsymbol{r}_{\mathrm{OD}}, \hat{\boldsymbol{n}}') \, \mathrm{d}\Omega' \tag{3.1}$$

3.2 Large scatterer approximation

The slab geometry is of interest in this paper, see Figure 6. The spheres are submerged in water between $0 \le z \le d$ or in terms of the scaled variables, $\tau = n_0\sigma_{\mathrm{ext}} z$, between $0 \le \tau \le \tau_0 = n_0\sigma_{\mathrm{ext}} d$. The scaled lateral variables are denoted $\boldsymbol{\eta} = n_0\sigma_{\mathrm{ext}}(x\hat{\boldsymbol{x}} + y\hat{\boldsymbol{y}})$.

[2] Other definitions occur — a factor of 4π differs and occasionally the scattering cross section is used instead of the extinction cross section.

[3] The independent variable is $\cos\theta = \hat{\boldsymbol{n}} \cdot \hat{\boldsymbol{n}}' = 1 - |\hat{\boldsymbol{n}} - \hat{\boldsymbol{n}}'|^2/2$.

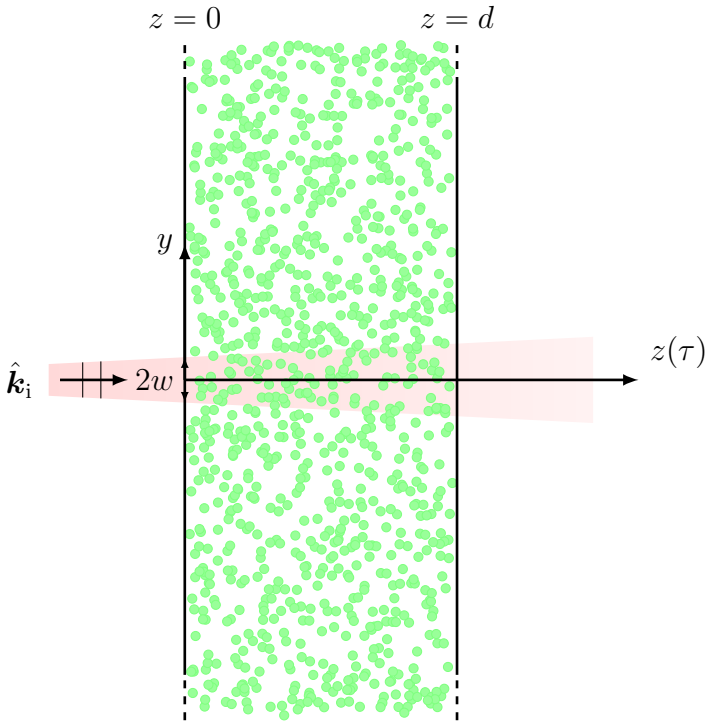

Figure 6: The geometry of a slab illuminated with a beam (laser sheet) of limited extent as seen from above. The width of the laser sheet at $\tau = 0$ is $2w$, and the direction of the exterior excitation is $\hat{\boldsymbol{k}}_{\mathrm{i}}$ (normal incidence).

The analysis reviewed in this section follows Ishimaru closely [12, Chapter 13] and [15]. An electrically large object scatters strongly in the forward direction, and less in all other directions. This fact motivates the large scatterer approximation, which neglects all scattering contributions except for a cone in the forward direction.

The direction $\hat{\boldsymbol{n}} = s_x\hat{\boldsymbol{x}} + s_y\hat{\boldsymbol{y}} + s_z\hat{\boldsymbol{z}}$, expressed in Cartesian coordinates, is subject to the constraint $s_x^2 + s_y^2 + s_z^2 = 1$. Most of the scattering takes place in the forward direction $s_z \approx 1$, *i.e.*, the scattering angle is always small. Therefore, the directional derivative is approximated with

$$\hat{\boldsymbol{n}} \cdot \nabla_{\mathrm{OD}} = s_z \frac{\partial}{\partial \tau} + \boldsymbol{s} \cdot \nabla_{\mathrm{OD}} \approx \frac{\partial}{\partial \tau} + \boldsymbol{s} \cdot \nabla_{\mathrm{OD}}$$

In the integral over the unit sphere, the lateral variable $\boldsymbol{s} = s_x\hat{\boldsymbol{x}} + s_y\hat{\boldsymbol{y}}$ is restricted by $s_x^2 + s_y^2 \leq 1$, but due to the vanishing contribution of the phase function when $s_x^2 + s_y^2 > 1$, the integration in $\boldsymbol{s}$ can be extended to the entire x-y plane, without a major change in the value of the integration.

As a consequence of the assumptions made above, the RTE in (3.1) is approximated by

$$\frac{\partial}{\partial \tau} I(\boldsymbol{\eta}, \tau, \boldsymbol{s}) + \boldsymbol{s} \cdot \nabla_{\mathrm{OD}} I(\boldsymbol{\eta}, \tau, \boldsymbol{s}) = -I(\boldsymbol{\eta}, \tau, \boldsymbol{s}) + \iint_{\mathbb{R}^2} p(\boldsymbol{s} - \boldsymbol{s}') I(\boldsymbol{\eta}, \tau, \boldsymbol{s}') \, \mathrm{d}\boldsymbol{s}'$$

where $\boldsymbol{s} = s_x\hat{\boldsymbol{x}} + s_y\hat{\boldsymbol{y}}$, $\boldsymbol{\eta} = n_0\sigma_{\text{ext}}(x\hat{\boldsymbol{x}} + y\hat{\boldsymbol{y}})$, $\tau = n_0\sigma_{\text{ext}}z$, and where the phase function $p(\boldsymbol{s} - \boldsymbol{s}')$ is[4]

$$p(\boldsymbol{s} - \boldsymbol{s}') \approx \frac{1}{4\pi\sigma_{\text{ext}}}\frac{\mathrm{d}\sigma}{\mathrm{d}\Omega}(\hat{\boldsymbol{n}} - \hat{\boldsymbol{n}}')$$

It is assumed that the phase function has its main contribution for small arguments $|\boldsymbol{s} - \boldsymbol{s}'|$.

Proceed by a Fourier transform of the RTE w.r.t. to $\boldsymbol{\eta}$. The result is

$$\frac{\mathrm{d}}{\mathrm{d}\tau}I(\boldsymbol{\kappa}, \tau, \boldsymbol{s}) = -(1 - \mathrm{i}\boldsymbol{s}\cdot\boldsymbol{\kappa})I(\boldsymbol{\kappa}, \tau, \boldsymbol{s}) + \iint\limits_{\mathbb{R}^2} p(\boldsymbol{s} - \boldsymbol{s}')I(\boldsymbol{\kappa}, \tau, \boldsymbol{s}')\ \mathrm{d}\boldsymbol{s}'$$

where

$$I(\boldsymbol{\kappa}, \tau, \boldsymbol{s}) = \iint\limits_{\mathbb{R}^2} I(\boldsymbol{\eta}, \tau, \boldsymbol{s})\mathrm{e}^{\mathrm{i}\boldsymbol{\kappa}\cdot\boldsymbol{\eta}}\ \mathrm{d}\boldsymbol{\eta}$$

with inverse

$$I(\boldsymbol{\eta}, \tau, \boldsymbol{s}) = \frac{1}{4\pi^2}\iint\limits_{\mathbb{R}^2} I(\boldsymbol{\kappa}, \tau, \boldsymbol{s})\mathrm{e}^{-\mathrm{i}\boldsymbol{\kappa}\cdot\boldsymbol{\eta}}\ \mathrm{d}\boldsymbol{\kappa}$$

A simplified notation is introduced to facilitate the analysis.

$$I(\boldsymbol{\kappa}, \tau, \boldsymbol{s}) = F(\boldsymbol{\kappa}, \tau, \boldsymbol{s})\mathrm{e}^{-(1-\mathrm{i}\boldsymbol{s}\cdot\boldsymbol{\kappa})\tau}$$

and $F(\boldsymbol{\kappa}, \tau, \boldsymbol{s})$ satisfies

$$\frac{\mathrm{d}}{\mathrm{d}\tau}F(\boldsymbol{\kappa}, \tau, \boldsymbol{s}) = \iint\limits_{\mathbb{R}^2} p(\boldsymbol{s} - \boldsymbol{s}')\mathrm{e}^{-\mathrm{i}(\boldsymbol{s}-\boldsymbol{s}')\cdot\boldsymbol{\kappa}\tau}F(\boldsymbol{\kappa}, \tau, \boldsymbol{s}')\ \mathrm{d}\boldsymbol{s}'$$

Now introduce the Fourier transform w.r.t. the variable $\boldsymbol{s}$. The following notation is used:

$$p(\boldsymbol{q}) = \iint\limits_{\mathbb{R}^2} p(\boldsymbol{s})\mathrm{e}^{\mathrm{i}\boldsymbol{q}\cdot\boldsymbol{s}}\ \mathrm{d}\boldsymbol{s}, \quad F(\boldsymbol{\kappa}, \tau, \boldsymbol{q}) = \iint\limits_{\mathbb{R}^2} F(\boldsymbol{\kappa}, \tau, \boldsymbol{s})\mathrm{e}^{\mathrm{i}\boldsymbol{q}\cdot\boldsymbol{s}}\ \mathrm{d}\boldsymbol{s}$$

with inverses

$$p(\boldsymbol{s}) = \frac{1}{4\pi^2}\iint\limits_{\mathbb{R}^2} p(\boldsymbol{q})\mathrm{e}^{-\mathrm{i}\boldsymbol{q}\cdot\boldsymbol{s}}\ \mathrm{d}\boldsymbol{q}, \quad F(\boldsymbol{\kappa}, \tau, \boldsymbol{s}) = \frac{1}{4\pi^2}\iint\limits_{\mathbb{R}^2} F(\boldsymbol{\kappa}, \tau, \boldsymbol{q})\mathrm{e}^{-\mathrm{i}\boldsymbol{q}\cdot\boldsymbol{s}}\ \mathrm{d}\boldsymbol{q}$$

Collecting the terms leads to the following differential equation

$$\frac{\mathrm{d}}{\mathrm{d}\tau}F(\boldsymbol{\kappa}, \tau, \boldsymbol{q}) = p(\boldsymbol{q} - \boldsymbol{\kappa}\tau)F(\boldsymbol{\kappa}, \tau, \boldsymbol{q})$$

The solution is (neglecting reflections at the back wall)

$$F(\boldsymbol{\kappa}, \tau, \boldsymbol{q}) = F(\boldsymbol{\kappa}, 0, \boldsymbol{q})\exp\left\{\int_0^\tau p(\boldsymbol{q} - \boldsymbol{\kappa}\tau')\ \mathrm{d}\tau'\right\}$$

[4]Holds as an approximation in the forward direction, and the phase function is assumed to depend only on $\boldsymbol{s} - \boldsymbol{s}'$ — in reality $|\hat{\boldsymbol{n}} - \hat{\boldsymbol{n}}'|^2 = |s_z\hat{\boldsymbol{z}} + \boldsymbol{s} - s_z'\hat{\boldsymbol{z}} - \boldsymbol{s}'|^2 \approx |\boldsymbol{s} - \boldsymbol{s}'|^2$.

To obtain the intensity, the inverse Fourier transforms in the variable $\boldsymbol{\kappa}$ and $\boldsymbol{q}$ are applied. The intensity in the slab at the location $(\boldsymbol{\eta}, \tau)$ in an arbitrary direction $\boldsymbol{s}$ is

$$I(\boldsymbol{\eta}, \tau, \boldsymbol{s}) = \frac{\mathrm{e}^{-\tau}}{16\pi^4} \iint_{\mathbb{R}^2} \iint_{\mathbb{R}^2} I(\boldsymbol{\kappa}, 0, \boldsymbol{q}) \mathrm{e}^{-\mathrm{i}(\boldsymbol{\eta} - \boldsymbol{s}\tau)\cdot\boldsymbol{\kappa} - \mathrm{i}\boldsymbol{q}\cdot\boldsymbol{s}} \cdot \exp\left\{ \int_0^\tau p(\boldsymbol{q} - \boldsymbol{\kappa}\tau') \, \mathrm{d}\tau' \right\} \mathrm{d}\boldsymbol{\kappa} \, \mathrm{d}\boldsymbol{q} \quad (3.2)$$

where

$$I(\boldsymbol{\kappa}, 0, \boldsymbol{q}) = \iint_{\mathbb{R}^2} I(\boldsymbol{\kappa}, 0, \boldsymbol{s}) \mathrm{e}^{\mathrm{i}\boldsymbol{q}\cdot\boldsymbol{s}} \, \mathrm{d}\boldsymbol{s}$$

Without any multiple scattering, $p(\boldsymbol{s}) = 0$, which implies that the exponential is replaced with one, and

$$I(\boldsymbol{\eta}, \tau, \boldsymbol{s}) = I(\boldsymbol{\eta} - \boldsymbol{s}\tau, 0, \boldsymbol{s}) \mathrm{e}^{-\tau}$$

The intensity in (3.2) models the intensity at the position $\boldsymbol{\eta}$ and depth τ in the direction $\boldsymbol{s}$. At this point this intensity excites the fluorescing dye, which has been added to the mixture to avoid the previously mentioned issues with Mie scattering detection (see Figure 5) and to improve the accuracy in the measuring process. To model the physics that we expect the SLIPI technique to be governed by, we ignore intensity contributions to the excitation of the fluorescing dye from all directions except the forward direction. Light contributions from other directions are not expected to carry the superimposed line structure used in SLIPI and are therefore removed in the data post-processing. In contrast, all light that maintains a straight path through the sample, despite being scattered on its way, will keep the structural imprint and, consequently, are unaffected by the SLIPI filtering. In the forward direction, $\boldsymbol{s} = \mathbf{0}$, the intensity is

$$I(\boldsymbol{\eta}, \tau, \mathbf{0}) = \frac{\mathrm{e}^{-\tau}}{16\pi^4} \iint_{\mathbb{R}^2} \iint_{\mathbb{R}^2} I(\boldsymbol{\kappa}, 0, \boldsymbol{q}) \mathrm{e}^{-\mathrm{i}\boldsymbol{\eta}\cdot\boldsymbol{\kappa}} \exp\left\{ \int_0^\tau p(\boldsymbol{q} - \boldsymbol{\kappa}\tau') \, \mathrm{d}\tau' \right\} \mathrm{d}\boldsymbol{\kappa} \, \mathrm{d}\boldsymbol{q} \quad (3.3)$$

This is the final expression of the intensity in the large scatterers approximation. For a given phase function $p(\boldsymbol{s})$, the two-fold inverse Fourier transform has to be performed to find the intensity $I(\boldsymbol{\eta}, \tau, \boldsymbol{s})$ or $I(\boldsymbol{\eta}, \tau, \mathbf{0})$.

If the background material is different, there is a reflection at $\tau = \tau_0$ with reflection coefficient R. The intensity close to the back wall in the forward direction is altered, and the total intensity at τ in the forward and backward directions, at the center $\boldsymbol{\eta} = \mathbf{0}$, is

$$I_{\text{total}}(\mathbf{0}, \tau, \mathbf{0}) = I(\mathbf{0}, \tau, \mathbf{0}) + RI(\mathbf{0}, \tau_0 - \tau, \mathbf{0})$$

3.3 Laser sheet

Assume the intensity at $\tau = 0$ has a Gaussian distribution in the $\boldsymbol{\eta} = \eta_y \hat{\boldsymbol{y}}$ direction with beam width[5] $2w$, and an angular spread at $\tau = 0$ modeled by the parameters σ_x and σ_y. The explicit form of the intensity at $\tau = 0$ is assumed to be

$$I(\boldsymbol{\eta}, 0, \boldsymbol{s}) = I_0 \sqrt{\frac{8}{\pi^3}} \frac{1}{w\sigma_x\sigma_y} \mathrm{e}^{-2\eta_y^2/w^2 - 2s_x^2/\sigma_x^2 - 2s_y^2/\sigma_y^2}$$

The parameter in the vertical direction, σ_x, shows little effect on the final result, but avoids a delta distribution in the coherent part of the intensity.

The constant I_0 is the total incident power flux per unit length in the vertical x direction, see Figure 6, since

$$\iint_{\mathbb{R}^2} \int_{-\infty}^{\infty} I(\boldsymbol{\eta}, 0, \boldsymbol{s}) \, \mathrm{d}\eta_y \, \mathrm{d}\boldsymbol{s} = I_0$$

This intensity characterizes the laser sheet, radiating in $\hat{\boldsymbol{z}}$, see also [16, 17, 18].

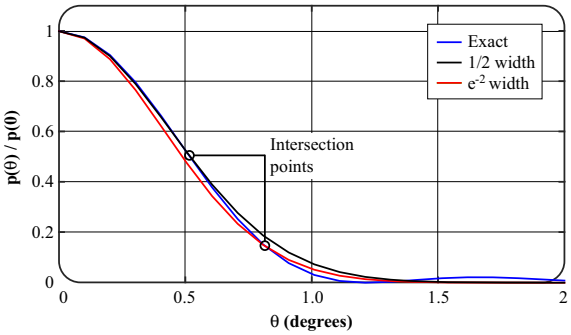

Figure 7: The normalized phase function $p(\theta)$ for a sphere with diameter $d = 24.90\,\mu$m. A comparison between the numerical (exact) and two approximate computations is depicted.

One critical point in the theory is the approximation of the phase function $p(\boldsymbol{s})$. This function is approximated by a Gaussian function, see Figure 7.

$$p(\boldsymbol{s}) = \frac{2\alpha}{\pi\beta^2} \mathrm{e}^{-2s^2/\beta^2}$$

where β is a measure of the width of the phase function in the forward direction (proportional to λ/D), and α is the single particle albedo. The normalization of the phase function is

$$\iint_{\Omega} p \, \mathrm{d}\Omega \approx \iint_{\mathbb{R}^2} p(\boldsymbol{s}) \, \mathrm{d}\boldsymbol{s} = \alpha$$

[5] The $1/\mathrm{e}^2$ beam width definition is used. If another beam width, say half intensity width $w_{1/2}$, is measured, let $w = w_{1/2}\sqrt{2/\ln 2}$ in the expressions. In the limit of zero beam width, a delta contribution is obtained.

The intensity in the $\boldsymbol{s}$ direction, see (3.2), is (details of the derivation are found in Appendix A)

$$I(\boldsymbol{\eta},\tau,\boldsymbol{s}) = \frac{I_0}{8\pi^3}\mathrm{e}^{-\tau}\iint\limits_{\mathbb{R}^2}\int_{-\infty}^{\infty}\mathrm{e}^{-\kappa_y^2 w^2/8 - q_y^2\sigma_y^2/8 - \mathrm{i}\kappa_y(\eta_y - s_y\tau) - \mathrm{i}\boldsymbol{q}\cdot\boldsymbol{s}} \cdot \exp\left\{\alpha\int_0^\tau \mathrm{e}^{-(q_x^2+(q_y-\kappa_y\tau')^2)\beta^2/8}\,\mathrm{d}\tau'\right\}\mathrm{d}\kappa_y\,\mathrm{d}\boldsymbol{q}$$

This expression quantifies the intensity in the laser sheet as a function of the lateral position $\boldsymbol{\eta}$ and depth τ in the direction $\boldsymbol{s}$. The intensity at the left hand side of the cuvette, $\tau = 0$, is assumed to have the following properties:

- No dependence of the vertical coordinate η_x.
- Gaussian beam shape of width $2w$ in the lateral direction η_y.
- The spread of the light intensity in the lateral direction is modeled with the constant σ_y.
- The spread of the light intensity in the vertical direction is modeled with the constant σ_x. It is convenient to give this parameter a non-zero value to avoid delta function contributions in the coherent contribution to the intensity.

From the general expression above, we identify two extreme cases, which are solved analytically.

1. If the multiple scattering can be neglected, $p(\boldsymbol{s}) = 0$, the intensity is

$$I(\boldsymbol{\eta},\tau,\boldsymbol{s}) = I((\eta_y - s_y\tau)\hat{\boldsymbol{y}},0,\boldsymbol{s})\mathrm{e}^{-\tau}$$

2. If the width of the phase function in the forward direction becomes infinitely small compared to the width parameter w (alternatively, the laser sheet is very wide), *i.e.*, let $\beta \to 0$, then

$$\begin{aligned} I(\boldsymbol{\eta},\tau,\boldsymbol{s}) &= \frac{I_0}{8\pi^3}\mathrm{e}^{-(1-\alpha)\tau}\iint\limits_{\mathbb{R}^2}\int_{-\infty}^{\infty}\mathrm{e}^{-\kappa_y^2 w^2/8 - q_x^2\sigma_x^2/8 - q_y^2\sigma_y^2/8 - \mathrm{i}\kappa_y(\eta_y - s_y\tau) - \mathrm{i}\boldsymbol{q}\cdot\boldsymbol{s}}\,\mathrm{d}\kappa_y\,\mathrm{d}\boldsymbol{q} \\ &= \mathrm{e}^{-(1-\alpha)\tau}I((\eta_y - s_y\tau)\hat{\boldsymbol{y}},0,\boldsymbol{s}) = \mathrm{e}^{-n_0\sigma_{\mathrm{a}}z}I((\eta_y - s_y\tau)\hat{\boldsymbol{y}},0,\boldsymbol{s}) \end{aligned}$$

where σ_{a} is the single particle absorption cross section.

3.3.1 The Wentzel summation method

To proceed, we apply the Wentzel method, see Appendix A. The result is

$$I(\boldsymbol{\eta},\tau,\boldsymbol{0}) = \sum_{m=0}^{\infty} I_m(\boldsymbol{\eta},\tau,\boldsymbol{0})$$

where, see (A.2)

$$I_m(\boldsymbol{\eta},\tau,\mathbf{0}) = I(\mathbf{0},0,\mathbf{0})\frac{\alpha^m}{m!}\mathrm{e}^{-\tau}A_m\int_0^\tau \mathrm{d}\tau_1\ldots\int_0^\tau \mathrm{d}\tau_m\frac{\mathrm{e}^{-2\eta_y^2/a_m}}{\sqrt{a_m}}$$

where the coefficients A_m are independent of $\tau_1,\ldots,\tau_m$

$$A_m = \frac{w\sigma_x\sigma_y}{\sqrt{\sigma_x^2+m\beta^2}\sqrt{\sigma_y^2+m\beta^2}}$$

and where

$$a_m = w^2+(\tau_1^2+\ldots+\tau_m^2)\beta^2-\frac{(\tau_1+\ldots+\tau_m)^2\beta^4}{\sigma_y^2+m\beta^2}$$

The term $m=0$ is assumed to contain no integration w.r.t. the τ variable.

The first three terms have explicit expressions in the forward direction $\boldsymbol{s}=\mathbf{0}$, see Appendix A.1.1. The first contribution, $m=0$, is the coherent contribution

$$I_0(\boldsymbol{\eta},\tau,\mathbf{0}) = I(\boldsymbol{\eta},0,\mathbf{0})\mathrm{e}^{-\tau} \tag{3.4}$$

and the second, $m=1$, is at the center of the laser sheet, $\eta_y=0$

$$I_1(\mathbf{0},\tau,\mathbf{0}) = I(\mathbf{0},0,\mathbf{0})\mathrm{e}^{-\tau}\frac{\alpha w\sigma_x}{\beta\sqrt{\sigma_x^2+\beta^2}}\mathrm{arcsinh}(\xi) \tag{3.5}$$

where

$$\xi = \frac{\beta\sigma_y\tau}{w\sqrt{\sigma_y^2+\beta^2}} = \frac{(\beta/w)}{\sqrt{1+(\beta/\sigma_y)^2}}\tau \tag{3.6}$$

The third term, $m=2$, at the center $\eta_y=0$ is

$$I_2(\mathbf{0},\tau,\mathbf{0}) = \frac{I_0\alpha^2}{2\pi^2}\mathrm{e}^{-\tau}\frac{1}{\sqrt{\sigma_x^2+2\beta^2}}\frac{1}{\sqrt{\sigma_y^2+2\beta^2}}\int_0^\tau \mathrm{d}\tau_1\int_0^\tau \mathrm{d}\tau_2\sqrt{\frac{8\pi}{a_2}}$$

where

$$a_2 = w^2+(\tau_1^2+\tau_2^2)\beta^2-\frac{(\tau_1+\tau_2)^2\beta^4}{\sigma_y^2+2\beta^2}$$

The higher order terms contain additional integration w.r.t. τ. A proof of the convergence of the Wentzel summation method is given in Appendix A.1.2. It is shown that the method always converges.

4 Results

To model the experimental results, the large scatterer approximation was used to solve the RTE. In particular, the Wentzel summation method was employed to find explicit results of the theoretical results. It was proved that this summation method always converges, and that sufficient accuracy is obtained with only a few terms. Specifically, the maximum error made by approximating the infinite sum in

M	0	1	2	3	4	5
$\Delta_M(\%)$	43	14	5.5	1.9	0.6	0.1

Table 2: The maximum error made in replacing the exact intensity by the first M terms in the Wentzel method for the largest sphere $d = 24.90\,\mu$m for the baseline parameters. This is the sphere size that produces the largest error.

d (μm)	4.518	5.94	11.00	15.66	18.79	24.90
β (rad)	0.0761	0.0606	0.0332	0.0232	0.0192	0.0145

Table 3: The calculated value of β in radians for each value of the diameter of the spheres. The e^{-2} width is given.

Wentzel summation method with just the M first term is displaced in Table 2, see Appendix A.1.3.

Comparing simulations and experiments would require exact knowledge of w, β, σ_x, and σ_y, which are difficult to assess experimentally with adequate accuracy. The correct value of β was obtained by Mie series calculations, see Table 3. Ten different simulations were therefore performed, each having a different set of input parameters, permitting us to find the settings which best agreed — qualitatively — with our SLIPI results. Note, however, that the aim of the current study is not achieving absolute agreement between experiments and simulations — this would require a more rigorous optical setup — but rather capturing and explaining the trends previously observed with SLIPI. The explicit values of the input parameters for the ten cases are given in Table 4.

No	1	2	3	4	5	**6**	7	8	9	10
w (μm)	50	50	100	100	200	**200**	300	300	400	400
σ_y (rad)	0.001	0.005	0.01	0.02	0.01	**0.02**	0.05	0.1	0.2	0.4

Table 4: The parameters in the comparison between theory and experiment. The vertical spread, σ_x, was set to 0.02 for all simulated cases. No 6, which gives the best agreement between simulations and experiments, is used as baseline in this paper.

Figure 8 displays the agreement between the SLIPI experiments and the ten simulated cases, compared by estimating the extinction of light along the x-direction (assuming a single exponential intensity decay). The fifth case gives the overall best agreement and is therefore referred to as the "baseline". Although deviations between experiments and simulations are observed even in the baseline case, both show a similar trend – as the particle size increases, the extinction reduces. Note that this is not in agreement with the Bouguer-Beer law, which predicts a constant extinction of 0.045 mm^{-1} for all particle sizes (dashed line). We consider the ability to reproduce this somewhat contradicting trend as a validation of the fidelity of our theoretical model and will now study its implications on extinction measurements

in more detail.

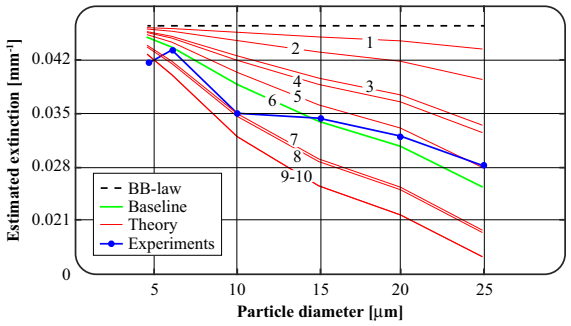

Figure 8: Comparison between the experiments and the ten simulated cases. To quantify the agreement, the extinction of light is estimated (in mm^{-1}). The extinction is estimated for $11 < x < 33$ mm, *i.e.*, in the center of the cuvette. The fifth case agrees best with the experimental data and is therefore set as a "baseline".

Our computations verify that the observed reduced extinction of light intensity couple to an increased forward-scattering for larger scatterers as was suggested by Kristensson *et al.* [7]. However, the model also reveals additional, rather unexpected factors that will affect experimental attempts to measure the extinction of light caused by scattering, namely the width of the laser sheet, w, and its spread along the y-direction, σ_y, (the spread along the x-direction, σ_x, was found to affect the outcome less). The influence of these factors can be seen in Figure 9, showing both experimental results and simulations for five different cases. Case 1 is considered an ideal measurement situation, having a thin laser sheet with a very low divergence — conditions which are, in principle, contradictory. The simulations still show a spread in the decay curves, *i.e.*, larger particles extinct light less effectively, yet the effect is not too pronounced and would probably be regarded as a measurement error if observed experimentally. Case 3 is a more realistic situation, where both the width of the laser sheet and its spreading along the x direction is slightly increased. The effect seen in case 1 is now augmented, showing a 85% higher intensity at $\tau = 2$ for the largest particles (25 μm) compared to the smallest one (4.5 μm). The "extreme" case — case 10 — displays strong deviations from the Bouguer-Beer law. Interestingly, the decay curves appears to be characterized by two stages; initially a weak reduction of light intensity is observed, followed by a more rapid one. Although not as apparent, the effect can also be observed in the experimental results. This characteristic can be understood by studying the incoherent contribution — the higher order M-terms. The local contribution from each M-term is illustrated in Figure 10, where the left graphs show the relative strength of each term as a function of OD. Here it can be observed how the $M = 1$ term steadily increase up to $OD \approx 0.6$, thus flattening the single exponential decay given by the coherent $M = 0$ term. The right graphs in Figure 10 show the contribution (in percentage) of each M-term relative to *all* light being detected. For 4.5 μm, the coherent $M = 0$ term is dominating, which explains why the model gives a good agreement with

the classic Bouguer-Beer relation for scattering upon smaller particles. However, as the particle size increases, higher M-terms are no longer negligible. At $OD = 2$ in the 25 μm case, the $M = 0$ term contributes merely with 41% (with respect to all detected light) and $M = 1$ with 32%, *i.e.*, their individual contributions are of similar magnitude and the incoherent contribution ($M \geqslant 1$ terms) is dominating. At $OD = 5$, the model predicts the four first M-terms to contribute with approximately equal magnitudes, for this particular case.

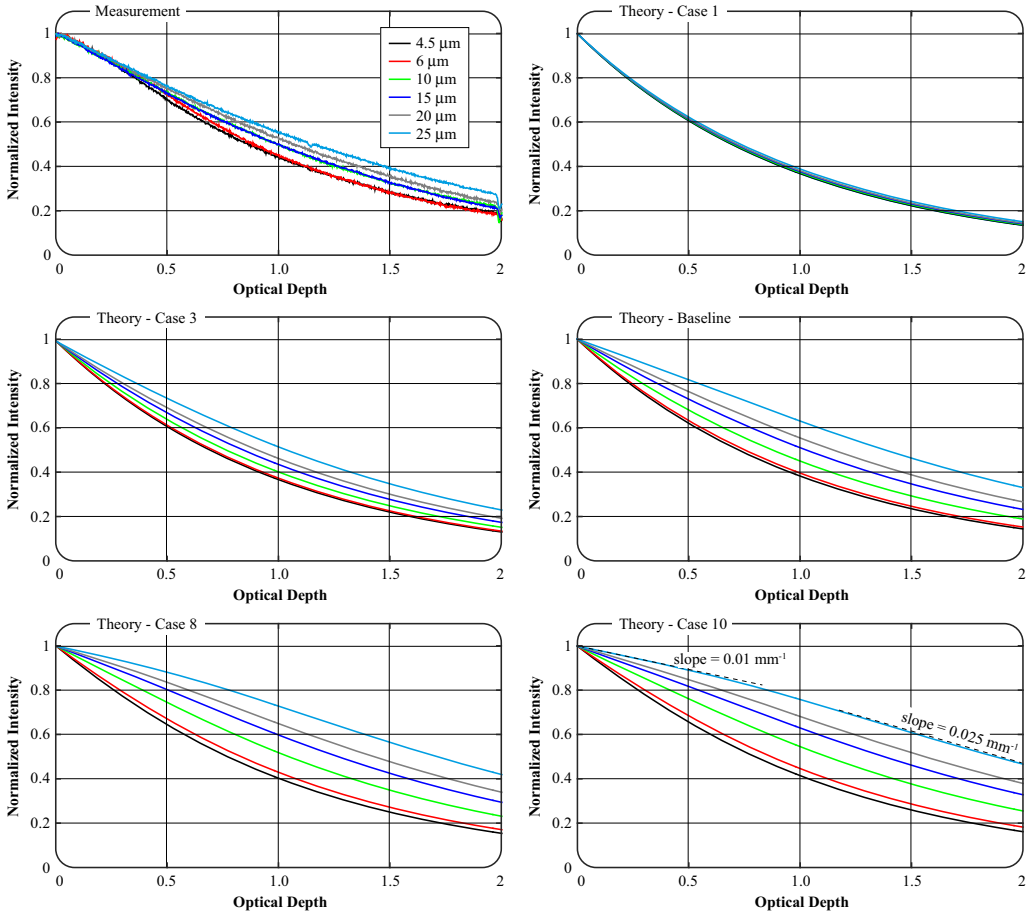

Figure 9: Results from experiments and five of the simulations, showing the local light intensity as a function of optical depth. The trend observed in the SLIPI data is clearly captured by the model, which further predicts significant deviations from the Bouguer-Beer law as the divergence as well as the thickness of the laser sheet increase.

From the results shown in Figure 8 and 9, it becomes clear that forward-scattering (*i.e.*, the β term) is not solely responsible for the observed deviations from the Bouguer-Beer law. Experimental factors, such as the thickness and the divergence of the laser sheet, are also important and will affect the outcome of a measurement. To investigate how these parameters influences the extinction of light, the sensitivity of the intensity w.r.t. the parameters w and σ_y were calculated, see Table 5. Note

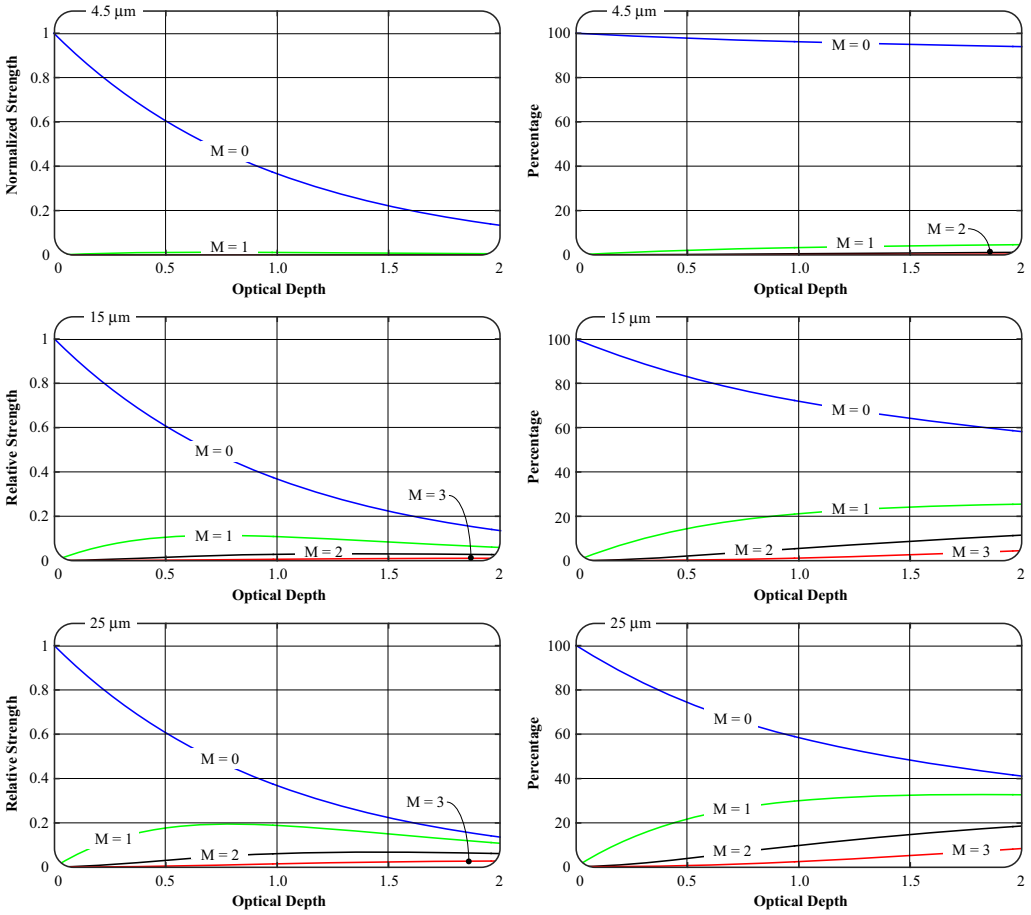

Figure 10: (Left graphs) The relative strength of each M-term as a function of OD for three particle sizes. Notice the local maxima of the $M = 1$ term around $OD \approx 0.6$, which explains the double-exponential decay observed in both experiments and simulations. (Right graphs) The contribution of each M-term as a function of OD, given in percentage. When light scatters upon small particles, the extinction of light follows the Bouguer-Beer law with sufficient accuracy (94% at $OD = 2$). This is no longer true for the 25 μm case, where the $M \geqslant 1$ terms (the incoherent contribution) are responsible for nearly 60% of the extinction at $OD = 2$. The calculations are based on the baseline parameters.

that the actual value of the derivative depends on the units that is used, which affects the interpretation of the results, and only relative comparisons in each column make sense.

The analysis shows that the intensity detected at a certain optical depth will vary depending on the width of the laser sheet and that the effect increases both with optical depth and particle size. Interestingly, the trend is somewhat different for the σ_y parameter; larger particles still give a higher variation in intensity at a given optical depth as σ_y varies (compared to smaller particles), but, in contrast, the effect is less pronounced at higher optical depths. The results may seem counterintuitive. However, two competing processes affect the intensity at a given OD. The coherent intensity — the Bouguer-Beer law — causes a divergence of the intensity that depends directly on the divergence of the intensity at $\tau = 0$, see (3.4). This agrees with the intuitive picture, that the intensity diverge more as the OD increases.

In contrast to this coherent contribution, the incoherent intensity — caused by multiple scattering — causes the intensity to line up in the forward direction, see Figure 1. This contribution has the opposite effect and reduces the divergence of the intensity. A closer look at the term $I_1(\mathbf{0}, \tau, \mathbf{0})$ in (3.5) also shows that the parameters w and σ_y in (3.6) are in the denominator and the numerator, respectively. The effect of these parameter w.r.t. the variation of the intensity at different OD therefore acts in the opposite direction. The higher OD, the more dominant the second, incoherent contribution becomes, see Figure 10, and it will eventually dominate over the coherent intensity, and the sensitivity w.r.t. variation in σ_y for higher OD follow the trend of the incoherent intensity.

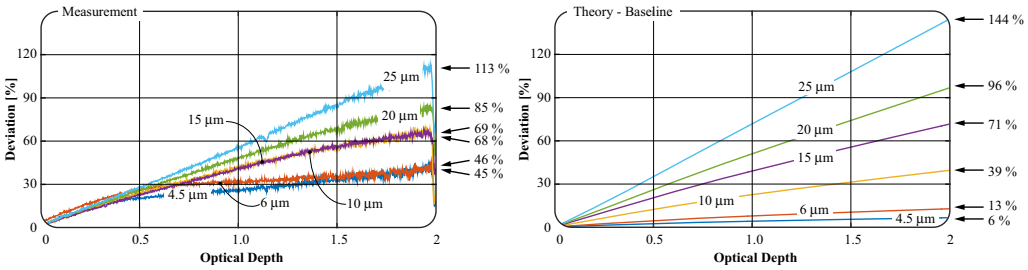

Figure 11: Deviations between the Bouguer-Beer law and the attenuation predicted by our model, given in percentage. The curves show that measurements performed on smaller particles agree better with the Bouguer-Beer law whereas measurements performed on larger particles give a significantly reduced extinction.

5 Discussion and conclusions

In summary, we have conducted SLIPI measurements in several turbid ($OD = 2$), scattering environments having monodisperse particle distributions with known concentrations. SLIPI was employed to suppress interferences caused by multiply scatte-

τ	d (μm)	$\partial_w I(\mu\text{m}^{-1})$	$\partial_{\sigma_y} I(\text{rad}^{-1})$
2	24.90	5.6	1.1
0.5	24.90	2.2	2.8
2	4.52	0.53	0.19
0.5	4.52	0.40	0.62

Table 5: The sensitivity of the normalized intensity $I(\mathbf{0}, \tau, \mathbf{0})/I(\mathbf{0}, 0, \mathbf{0})$ for two different depths (τ) and two particle sizes (d), for the baseline parameters. The intensity is approximated by the first two terms in Wentzel summation method, *i.e.*, $I(\mathbf{0}, \tau, \mathbf{0}) = I_0(\mathbf{0}, \tau, \mathbf{0}) + I_1(\mathbf{0}, \tau, \mathbf{0})$.

red light that otherwise make imaging in such turbid situations difficult, permitting us to visualize the local extinction of light from the side. A theoretical model was developed that calculates how a laser sheet is transferred through such scattering environments. The model uses the large scatterer approximation to solve the Radiative Transfer Equation, yet has additional constrains to best model the SLIPI process. Light that diverges from its initial trajectory during a scattering event is suppressed by the SLIPI technique. However, should the initial trajectory be maintained as light scatters upon the spherical, non-absorbing particles, its energy is unaffected. This effect, which influences other measurement techniques as well, was included in the model (see Equation 3.3).

The experiments and the theoretical predictions are in good agreement, both clearly showing how the current conception of light extinction — the Bouguer-Beer law — is not completely accurate in these turbid environments from an experimental perspective. For example, the model shows that the measurable opacity of a homogeneous sample with particles of 25 μm in diameter is reduced by roughly 140% at an (expected) optical depth of 2 — a deviation that should be considered in quantitative measurements that are based on light attenuation caused partly or entirely by scattering. The deviation from the Bougour-Beer law is illustrated in Figure 11.

Another interesting finding revealed by the model concerns the incoherent contribution, which can be expressed as a summation of infinitely many terms of varying *local* strengths (see Figure 10). These are thus fundamentally different from the coherent contribution — the Bouguer-Beer relation — that predicts light to decay as a single exponential. When probing small particles (and/or at a low opacity), higher order M-terms are negligible, whereas they grow in magnitude for samples containing relatively large scattering particles. Experimentally, this can be observed as a reduced extinction initially (contribution from $M = 1$), followed by a more rapid decay (see Figure 9).

We have summarized the main discoveries of the current study below:

- Probing turbid, scattering samples having different monodisperse particle sizes but (theoretically) equal opacities leads to measurable differences in terms of light extinction.

- For a given OD, samples with larger particles appear less opaque, *i.e.*, they

transmit more light. This, in turn, is beneficial in terms of visualization, yet may render difficulties making quantitative assessments.

- The Bouguer-Beer law in its current form does not take the preservation of the energy in the forward direction into account. Experimentally, unperturbed- and forward-scattered light can be very difficult (if possible) to differentiate.

- Light energy being preserved in the forward direction is not a unique concern for SLIPI measurements but should be classified as a *general* light-matter interaction feature, affecting, in principle, all light-based probing techniques employed in scattering environments.

- The thickness as well as the lateral divergence of the laser sheet also affects the magnitude of the deviations from the Bouguer-Beer law.

- The thicker the laser sheet, the less the light extinction. In the extreme case (infinite thickness), scattering losses are negligible and only extinction due to absorption can be detected. The magnitude of this effect increases with optical depth.

- The higher the divergence of the laser sheet, the less the light extinction. However, the magnitude of this effect decreases with optical depth.

- The incoherent contribution that maintains the incident trajectory can be expressed as a sum of infinitely many terms. The coherent contribution (the Bouguer-Beer relation) is only the first of these terms.

- Different terms contribute differently and, for example, the shape of the second term explains the initially lower extinction that has been observed experimentally.

- The coherent term ($M = 0$) describes the intensity *losses* occurring within the sample whereas the incoherent terms ($M \geqslant 1$) describes the positive intensity *contributions* caused by forward-scattering.

To the best of our knowledge, the trends presented in this study have not been observed in the past, which we believe is due to two factors. First, the deviation from the Bouguer-Beer law is not observed at low optical depths and imaging through/in turbid media is associated with a great experimental difficulty. Only a few optical methods with this capacity do exist, SLIPI being one of them. Ballistic imaging [19], which is used both for tissue imaging and for spray visualization, has the capability of visualizing thorough strongly scattering media, yet provides "only" line-of-sight information. Since the effects discovered in this study are occurring locally within the sample, they are unlikely to be observed with line-of-sight techniques. Second, measurements based on side-scattering detection of light in scattering environments are often deteriorated by out-of-plane contributions stemming from multiple light scattering. The effects discovered in this study are probably to minute in comparison to have been observed using such conventional techniques.

Despite a generally good agreement between experiments and our theoretical model, there are, however, several sources of error that should be addressed. First, since the particle number density varied between samples, so did the accuracy on the concentration. This could potentially generate similar trends as those observed, yet we find this scenario unlikely. Second, unlike simulations, experimental measurements face obstacles such as a limited dynamic range, detector noise, laser power fluctuations, *etc.*, which will affect the fidelity of the measurements and thereby also the agreement with simulations. Third, the initial flattened decay that we believe to be coupled with the first incoherent term could also be caused by vignetting, although measures were taken to minimize it (using a small collection angle).

In the companion paper we expand the theoretical model to further include the sinusoidal modulation in the SLIPI laser sheet intensity profile and we compare simulations with measurements, where the spatial frequency of the modulation is altered in a controlled fashion. The aim of the study is to investigate if and to what magnitude the modulation frequency of the SLIPI laser sheet affects the fidelity of a measurement of a scattering environment.

Appendix A Laser sheet (Gaussian shape)

This appendix contains the details of the computations of the intensity for an incident intensity at $\tau = 0$ of Gaussian form. Moreover, the phase function is also assumed to have a Gaussian distribution. These approximations are reasonable for the problem under consideration.

The intensity of the incident laser sheet at $\tau = 0$ is (no dependence on the vertical coordinate η_x) simulates a laser sheet of width $2w$.

$$I(\boldsymbol{\eta}, 0, \boldsymbol{s}) = I_0 \sqrt{\frac{8}{\pi^3}} \frac{1}{w\sigma_x\sigma_y} \mathrm{e}^{-2\eta_y^2/w^2 - 2s_x^2/\sigma_x^2 - 2s_y^2/\sigma_y^2}$$

The intensity contains two spread parameters, σ_x and σ_y, which models the divergence of the light intensity. The parameter in the vertical direction, σ_x, has little effect on the final result, but is set to a non-zero value to avoid a delta distribution in the coherent contribution.

The Fourier transform is easily computed, see Appendix B.

$$I(\boldsymbol{\kappa}, 0, \boldsymbol{q}) = \iint\limits_{\mathbb{R}^2} \iint\limits_{\mathbb{R}^2} I(\boldsymbol{\eta}, 0, \boldsymbol{s}) \mathrm{e}^{\mathrm{i}\boldsymbol{\kappa}\cdot\boldsymbol{\eta} + \mathrm{i}\boldsymbol{q}\cdot\boldsymbol{s}} \, \mathrm{d}\boldsymbol{\eta} \, \mathrm{d}\boldsymbol{s} = I_0 2\pi\delta(\kappa_x) \mathrm{e}^{-\kappa_y^2 w^2/8 - q_x^2\sigma_x^2/8 - q_y^2\sigma_y^2/8}$$

The phase function is approximated by a Gaussian function.

$$p(\boldsymbol{s}) = \frac{2\alpha}{\pi\beta^2} \mathrm{e}^{-2s^2/\beta^2}$$

The Fourier transform of the phase function is

$$p(\boldsymbol{q}) = \frac{2\alpha}{\pi\beta^2} \iint\limits_{\mathbb{R}^2} \mathrm{e}^{-2s^2/\beta^2 + \mathrm{i}\boldsymbol{q}\cdot\boldsymbol{s}} \, \mathrm{d}\boldsymbol{s} = \alpha \mathrm{e}^{-q^2\beta^2/8}$$

The intensity in the $\boldsymbol{s}$ direction, see (3.2), is

$$I(\boldsymbol{\eta},\tau,\boldsymbol{s}) = \frac{I_0}{8\pi^3}\mathrm{e}^{-\tau}\iint\limits_{\mathbb{R}^2}\int_{-\infty}^{\infty}\mathrm{e}^{-\kappa_y^2w^2/8-q_x^2\sigma_x^2/8-q_y^2\sigma_y^2/8-\mathrm{i}\kappa_y(\eta_y-s_y\tau)-\mathrm{i}\boldsymbol{q}\cdot\boldsymbol{s}} \cdot\exp\left\{\alpha\int_0^\tau \mathrm{e}^{-(q_x^2+(q_y-\kappa_y\tau')^2)\beta^2/8}\,\mathrm{d}\tau'\right\}\mathrm{d}\kappa_y\,\mathrm{d}\boldsymbol{q}$$

This is the general expression of the intensity in the laser sheet.

A.1 The Wentzel summation method

To proceed with the general case, expand the exponent in a power series.

$$\exp\left\{\alpha\int_0^\tau \mathrm{e}^{-(q_x^2+(q_y-\kappa_y\tau')^2)\beta^2/8}\,\mathrm{d}\tau'\right\} = \sum_{m=0}^{\infty}\frac{\alpha^m}{m!}\mathrm{e}^{-mq_x^2\beta^2/8}\left\{\int_0^\tau \mathrm{e}^{-(q_y-\kappa_y\tau')^2\beta^2/8}\,\mathrm{d}\tau'\right\}^m$$

and evaluate the $\boldsymbol{q}$ and κ_y integrations in the calculations of the intensity first. This method was suggested by Wentzel [17, 20, 21] in a different application, but is here used to explicitly calculate an approximate value of the intensity $I(\boldsymbol{\eta},\tau,\boldsymbol{s})$. In essence, the method divides the intensity into an infinite series of contributions — the more terms, the more accurate approximation.

$$I(\boldsymbol{\eta},\tau,\boldsymbol{s}) = \sum_{m=0}^{\infty} I_m(\boldsymbol{\eta},\tau,\boldsymbol{s}) \tag{A.1}$$

where

$$I_m(\boldsymbol{\eta},\tau,\boldsymbol{s}) = \frac{I_0\alpha^m}{8\pi^3 m!}\mathrm{e}^{-\tau}\int_0^\tau \mathrm{d}\tau_1\ldots\int_0^\tau \mathrm{d}\tau_m\int_{-\infty}^{\infty}\mathrm{d}\kappa_y\iint\limits_{\mathbb{R}^2}\mathrm{d}\boldsymbol{q} \cdot\mathrm{e}^{-\kappa_y^2w^2/8-q_x^2\sigma_x^2/8-q_y^2\sigma_y^2/8-\mathrm{i}\kappa_y(\eta_y-s_y\tau)-\mathrm{i}\boldsymbol{q}\cdot\boldsymbol{s}-mq_x^2\beta^2/8-(q_y-\kappa_y\tau_1)^2\beta^2/8-\ldots-(q_y-\kappa_y\tau_m)^2\beta^2/8}$$

The term $m=0$ is assumed to contain no integration w.r.t. the τ variable. Explicitly, the $m=0$ term is

$$I_0(\boldsymbol{\eta},\tau,\boldsymbol{s}) = \frac{I_0}{8\pi^3}\mathrm{e}^{-\tau}\int_{-\infty}^{\infty}\mathrm{d}\kappa_y\iint\limits_{\mathbb{R}^2}\mathrm{d}\boldsymbol{q}\,\mathrm{e}^{-\kappa_y^2w^2/8-q_x^2\sigma_x^2/8-q_y^2\sigma_y^2/8-\mathrm{i}\kappa_y(\eta_y-s_y\tau)-\mathrm{i}\boldsymbol{q}\cdot\boldsymbol{s}}$$
$$= \mathrm{e}^{-\tau}I_0\sqrt{\frac{8}{\pi^3}}\frac{1}{w\sigma_x\sigma_y}\mathrm{e}^{-2(\eta_y-s_y\tau)^2/w^2-2s_x^2/\sigma_x^2-2s_y^2/\sigma_y^2} = I((\eta_y-s_y\tau)\hat{\boldsymbol{y}},0,\boldsymbol{s})\mathrm{e}^{-\tau}$$

The first term $I_0(\boldsymbol{\eta},\tau,\boldsymbol{s})$ shows a damping and a broadening of the intensity at $\tau=0$. The $m=0$ term is the coherent contribution to the intensity in the laser sheet, and

the higher order terms, $m = 1, 2, \ldots$, are incoherent, or diffuse, contributions. This zero order term is also the complete solution if there are no scatterers present.

Simplify the exponent in the general expression for $m = 1, 2, \ldots$.

$$I_m(\boldsymbol{\eta}, \tau, \boldsymbol{s}) = \frac{I_0 \alpha^m}{8\pi^3 m!} \mathrm{e}^{-\tau} \int_0^\tau \mathrm{d}\tau_1 \ldots \int_0^\tau \mathrm{d}\tau_m \int_{-\infty}^{\infty} \mathrm{d}\kappa_y \iint\limits_{\mathbb{R}^2} \mathrm{d}\boldsymbol{q}$$
$$\cdot \, \mathrm{e}^{-\kappa_y^2(w^2+(\tau_1^2+\ldots+\tau_m^2)\beta^2)/8 - q_x^2(\sigma_x^2+m\beta^2)/8 - q_y^2(\sigma_y^2+m\beta^2)/8 - \mathrm{i}\kappa_y(\eta_y - s_y\tau) - \mathrm{i}\boldsymbol{q}\cdot\boldsymbol{s} + q_y\kappa_y(\tau_1+\ldots+\tau_m)\beta^2/4}$$

In the forward direction, $\boldsymbol{s} = \boldsymbol{0}$, the expression simplifies to

$$I_m(\boldsymbol{\eta}, \tau, \boldsymbol{0}) = \frac{I_0 \alpha^m}{8\pi^3 m!} \mathrm{e}^{-\tau} \int_0^\tau \mathrm{d}\tau_1 \ldots \int_0^\tau \mathrm{d}\tau_m \int_{-\infty}^{\infty} \mathrm{d}\kappa_y \iint\limits_{\mathbb{R}^2} \mathrm{d}\boldsymbol{q}$$
$$\cdot \, \mathrm{e}^{-\kappa_y^2(w^2+(\tau_1^2+\ldots+\tau_m^2)\beta^2)/8 - q_x^2(\sigma_x^2+m\beta^2)/8 - q_y^2(\sigma_y^2+m\beta^2)/8 - \mathrm{i}\kappa_y\eta_y + q_y\kappa_y(\tau_1+\ldots+\tau_m)\beta^2/4}$$

The q_x and q_y integrations give

$$I_m(\boldsymbol{\eta}, \tau, \boldsymbol{0}) = \frac{I_0 \alpha^m}{8\pi^3 m!} \mathrm{e}^{-\tau} \sqrt{\frac{8\pi}{\sigma_x^2 + m\beta^2}} \sqrt{\frac{8\pi}{\sigma_y^2 + m\beta^2}} \int_0^\tau \mathrm{d}\tau_1 \ldots \int_0^\tau \mathrm{d}\tau_m \int_{-\infty}^{\infty} \mathrm{d}\kappa_y$$
$$\cdot \, \mathrm{e}^{-\kappa_y^2(w^2+(\tau_1^2+\ldots+\tau_m^2)\beta^2)/8 + \kappa_y^2(\tau_1+\ldots+\tau_m)^2\beta^4/(8(\sigma_y^2+m\beta^2)) - \mathrm{i}\kappa_y\eta_y}$$

and the κ_y integration entails

$$I_m(\boldsymbol{\eta}, \tau, \boldsymbol{0}) = I(\boldsymbol{0}, 0, \boldsymbol{0}) \frac{\alpha^m}{m!} \mathrm{e}^{-\tau} A_m \int_0^\tau \mathrm{d}\tau_1 \ldots \int_0^\tau \mathrm{d}\tau_m \frac{\mathrm{e}^{-2\eta_y^2/a_m}}{\sqrt{a_m}} \tag{A.2}$$

where the coefficients A_m are independent of $\tau_1, \ldots, \tau_m$, given by

$$A_m = \frac{w\sigma_x\sigma_y}{\sqrt{\sigma_x^2 + m\beta^2}\sqrt{\sigma_y^2 + m\beta^2}}$$

and where

$$a_m = w^2 + (\tau_1^2 + \ldots + \tau_m^2)\beta^2 - \frac{(\tau_1 + \ldots + \tau_m)^2\beta^4}{\sigma_y^2 + m\beta^2}$$

The sequence $\{A_m\}_{m=1}^\infty$ is a decreasing sequence

$$w = A_0 > \ldots > A_m > A_{m+1}, \quad m = 1, 2, 3, \ldots$$

Note that the factors a_m are always positive, since (let $p = 2$ in (C.1), $\tau_i \geq 0$, $i = 1, \ldots, m$)

$$m \sum_{i=1}^m \tau_i^2 \geq \left(\sum_{i=1}^m \tau_i \right)^2, \quad m = 1, 2, \ldots$$

which implies

$$a_m \geq w^2 + (\tau_1^2 + \ldots + \tau_m^2)\beta^2 - \frac{m(\tau_1^2 + \ldots + \tau_m^2)\beta^4}{\sigma_y^2 + m\beta^2}$$
$$= w^2 + \beta^2(\tau_1^2 + \ldots + \tau_m^2)\frac{\sigma_y^2}{\sigma_y^2 + m\beta^2} \geq 0$$

Moreover, the sequence $\{a_m\}_{m=1}^{\infty}$ is an increasing sequence in m if all other parameters are kept fixed. In fact, using the inequality in Appendix C.2 ($x = (\tau_1 + \ldots + \tau_m)\beta$, $y = \tau_{m+1}\beta$, and $a = \sigma_y^2/\beta^2$) implies

$$\begin{aligned} w^2 = a_0 \leq \ldots \leq a_m \leq a_m \\ + \tau_{m+1}^2\beta^2 + \frac{(\tau_1 + \ldots + \tau_m)^2\beta^4}{\sigma_y^2 + m\beta^2} - \frac{(\tau_1 + \ldots + \tau_m + \tau_{m+1})^2\beta^4}{\sigma_y^2 + (m+1)\beta^2} = a_{m+1} \end{aligned}$$

with equality when $(\tau_1 + \ldots + \tau_m)\beta = \tau_{m+1}\beta(\sigma_y^2/\beta^2 + m)$.

A.1.1 Evaluation of terms

The first two contributions in the series can be evaluated analytically. The first term, $m = 0$, in Equation (A.2), is the coherent contribution

$$I_0(\boldsymbol{\eta}, \tau, \mathbf{0}) = I(\boldsymbol{\eta}, 0, \mathbf{0})\mathrm{e}^{-\tau}$$

and the second, $m = 1$, is

$$I_m(\boldsymbol{\eta}, \tau, \mathbf{0}) = I(\mathbf{0}, 0, \mathbf{0})\alpha\mathrm{e}^{-\tau}A_1 \int_0^{\tau} \mathrm{d}\tau_1 \frac{\mathrm{e}^{-2\eta_y^2/a_1}}{\sqrt{a_1}}$$

$$A_1 = \frac{w\sigma_x\sigma_y}{\sqrt{\sigma_x^2 + \beta^2}\sqrt{\sigma_y^2 + \beta^2}}$$

and where

$$a_1 = w^2 + \tau_1^2\beta^2 - \frac{\tau_1^2\beta^4}{\sigma_y^2 + \beta^2} = w^2 + \frac{\tau_1^2\beta^2\sigma_y^2}{\sigma_y^2 + \beta^2}$$

At the center of the laser sheet, $\eta_y = 0$, the term is evaluated in elementary functions, see Appendix B

$$I_1(\mathbf{0}, \tau, \mathbf{0}) = I(\mathbf{0}, 0, \mathbf{0})\mathrm{e}^{-\tau}\frac{\alpha w\sigma_x}{\beta\sqrt{\sigma_x^2 + \beta^2}}\mathrm{arcsinh}(\xi)$$

where

$$\xi = \frac{\beta\sigma_y\tau}{w\sqrt{\sigma_y^2 + \beta^2}}$$

The third term, $m = 2$, at the center $\eta_y = 0$ is

$$I_2(\boldsymbol{\eta}, \tau, \mathbf{0}) = I(\mathbf{0}, 0, \mathbf{0})\frac{\alpha^2}{2}\mathrm{e}^{-\tau}\frac{w\sigma_x\sigma_y}{\sqrt{\sigma_x^2 + 2\beta^2}\sqrt{\sigma_y^2 + 2\beta^2}}\int_0^{\tau}\mathrm{d}\tau_1\int_0^{\tau}\mathrm{d}\tau_2\frac{\mathrm{e}^{-2\eta_y^2/a_2}}{\sqrt{a_2}}$$

where

$$a_2 = w^2 + (\tau_1^2 + \tau_2^2)\beta^2 - \frac{(\tau_1 + \tau_2)^2\beta^4}{\sigma_y^2 + 2\beta^2}$$

This term has to be integrated numerically. The integrand is well-behaved and the numerical integration can easily be performed without any problems.

A.1.2 Proof of convergence

In this appendix the Wentzel summation method is proved to converge. To accomplish this, we utilize that the sequence $\{a_m\}_{m=1}^{\infty}$ is an increasing sequence in m if all other parameters are kept fixed, and that sequence $\{A_m\}_{m=1}^{\infty}$ is an decreasing sequence in m. These facts prove the convergence of the Wentzel summation method in the forward direction $\boldsymbol{s} = \mathbf{0}$. The intensity at the position η_y and τ is, see (A.2)

$$I(\boldsymbol{\eta}, \tau, \mathbf{0}) = I(\mathbf{0}, 0, \mathbf{0})\mathrm{e}^{-\tau} \sum_{m=0}^{\infty} A_m \frac{\alpha^m}{m!} \int_0^{\tau} \mathrm{d}\tau_1 \ldots \int_0^{\tau} \mathrm{d}\tau_m \frac{\mathrm{e}^{-2\eta_y^2/a_m}}{\sqrt{a_m}}$$

In fact, the positive series is bounded, *i.e.*,

$$\begin{aligned} I(\boldsymbol{\eta}, \tau, \mathbf{0}) &\leq I(\mathbf{0}, 0, \mathbf{0})\mathrm{e}^{-\tau} \sum_{m=0}^{\infty} A_0 \frac{\alpha^m}{m!} \int_0^{\tau} \mathrm{d}\tau_1 \ldots \int_0^{\tau} \mathrm{d}\tau_m \frac{1}{\sqrt{a_0}} \\ &= I(\mathbf{0}, 0, \mathbf{0})\mathrm{e}^{-\tau} \sum_{m=0}^{\infty} \frac{(\tau\alpha)^m}{m!} = I(\mathbf{0}, 0, \mathbf{0})\mathrm{e}^{-\tau(1-\alpha)} \leq I(\mathbf{0}, 0, \mathbf{0}) \end{aligned}$$

which is a finite quantity. Since all terms in the Wentzel summation method are real and positive, this estimate proves the convergence.

A.1.3 Estimate of error

Let Δ_M denote the error made in the computation of the intensity in the forward direction, $\boldsymbol{s} = \mathbf{0}$, if the first M terms are included in the Wentzel summation method. Since the sum in (A.1) converges, the error is

$$\Delta_M = I(\mathbf{0}, 0, \mathbf{0})\mathrm{e}^{-\tau} \sum_{m=M+1}^{\infty} \frac{\alpha^m}{m!} A_m \int_0^{\tau} \mathrm{d}\tau_1 \ldots \int_0^{\tau} \mathrm{d}\tau_m \frac{\mathrm{e}^{-2\eta_y^2/a_m}}{\sqrt{a_m}}$$

where

$$a_m = w^2 + (\tau_1^2 + \ldots + \tau_m^2)\beta^2 - \frac{(\tau_1 + \ldots + \tau_m)^2\beta^4}{\sigma_y^2 + m\beta^2}$$

The largest error occurs at $\eta_y = 0$.

$$\Delta_M \leq I(\mathbf{0}, 0, \mathbf{0})\mathrm{e}^{-\tau} \sum_{m=M+1}^{\infty} \frac{\alpha^m}{m!} \frac{w\sigma_x\sigma_y}{\sqrt{\sigma_x^2 + m\beta^2}\sqrt{\sigma_y^2 + m\beta^2}} \int_0^{\tau} \mathrm{d}\tau_1 \ldots \int_0^{\tau} \mathrm{d}\tau_m \frac{1}{\sqrt{a_m}}$$

For fixed m apply the inequality in Appendix C with $p = 2$. The result is

$$\begin{aligned} a_m &= w^2 + \beta^2 \frac{(\tau_1^2 + \ldots + \tau_m^2)(\sigma_y^2 + m\beta^2) - (\tau_1 + \ldots + \tau_m)^2\beta^2}{\sigma_y^2 + m\beta^2} \\ &\geq w^2 + (\tau_1^2 + \ldots + \tau_m^2)\frac{\beta^2\sigma_y^2}{\sigma_y^2 + m\beta^2} \\ &= \frac{\beta^2\sigma_y^2}{\sigma_y^2 + m\beta^2}\left(\frac{w^2(\sigma_y^2 + m\beta^2)}{\beta^2\sigma_y^2} + \tau_1^2 + \ldots + \tau_m^2\right) \end{aligned}$$

and the error is

$$\Delta_M \le I(\mathbf{0},0,\mathbf{0})\mathrm{e}^{-\tau}\sum_{m=M+1}^{\infty}\frac{\alpha^m}{m!}\frac{w\sigma_x}{\beta\sqrt{\sigma_x^2+m\beta^2}} \times\int_0^\tau \mathrm{d}\tau_1\ldots\int_0^\tau \mathrm{d}\tau_m\frac{1}{\sqrt{\frac{w^2(\sigma_y^2+m\beta^2)}{\beta^2\sigma_y^2}+\tau_1^2+\ldots+\tau_m^2}}$$

Estimate the denominator from below.

$$\Delta_M \le I(\mathbf{0},0,\mathbf{0})\mathrm{e}^{-\tau}\frac{w\sigma_x}{\beta\sqrt{\sigma_x^2+(M+1)\beta^2}}\sum_{m=M+1}^{\infty}\frac{\alpha^m}{m!} \times\tau^{m-M}\int_0^\tau \mathrm{d}\tau_1\ldots\int_0^\tau \mathrm{d}\tau_M\frac{1}{\sqrt{\frac{w^2(\sigma_y^2+(M+1)\beta^2)}{\beta^2\sigma_y^2}+\tau_1^2+\ldots+\tau_M^2}}$$

or

$$\Delta_M \le I(\mathbf{0},0,\mathbf{0})\mathrm{e}^{-\tau}\frac{w\sigma_x}{\beta\sqrt{\sigma_x^2+(M+1)\beta^2}}\tau^{-M} \times\int_0^\tau \mathrm{d}\tau_1\ldots\int_0^\tau \mathrm{d}\tau_M\frac{1}{\sqrt{\frac{w^2(\sigma_y^2+(M+1)\beta^2)}{\beta^2\sigma_y^2}+\tau_1^2+\ldots+\tau_M^2}}\underbrace{\sum_{m=M+1}^{\infty}\frac{(\alpha\tau)^m}{m!}}_{\mathrm{e}^{\alpha\tau}-\sum_{m=0}^{M}\frac{(\alpha\tau)^m}{m!}}$$

It is easy to prove that this error, viewed as a function of τ, attains its maximum value at $\tau=\tau_0$.

Appendix B Useful integrals

A few of the pertinent integrals are listed here, see page 337 (3.323) in Ref [22].

$$\int_{-\infty}^{\infty}\mathrm{e}^{-2x^2/a^2\pm bx}\,\mathrm{d}x = a\sqrt{\frac{\pi}{2}}\mathrm{e}^{a^2b^2/8},\quad \mathrm{Re}\,a^2>0$$

Another useful integral is [22, page 94 (2.261)].

$$\int\frac{\mathrm{d}x}{\sqrt{a^2+b^2x^2}} = \frac{1}{b}\mathrm{arcsinh}\left(\frac{bx}{a}\right)$$

Appendix C Inequalities

A few important inequalities are employed in the paper. In this appendix these inequalities are proved.

C.1 Inequality 1

Let $1 \leq p < \infty$ and m a positive integer. Then

$$\left(\sum_{i=1}^{m} x_i\right)^p \leq m^{p-1} \sum_{i=1}^{m} x_i^p, \qquad x \in \mathbb{R}_+^m \tag{C.1}$$

This inequality is proved by induction in m. For $m = 1$ we have the trivial inequality

$$x_1^p \leq x_1^p$$

Next assume the inequality is correct for $m = 1, 2, \ldots, k$, and prove the inequality for $m = k + 1$. To this end, define

$$f(x) = (k+1)^{p-1} \sum_{i=1}^{k+1} x_i^p - \left(\sum_{i=1}^{k+1} x_i\right)^p, \quad x = (x_1, x_2, \ldots, x_{k+1}) \in \mathbb{R}_+^{k+1}$$

and prove that $f(x) \geq 0$ in $x \in \mathbb{R}_+^{k+1}$. Especially, due to the induction assumption

$$k^{p-1} \sum_{i=1}^{k} x_i^p - \left(\sum_{i=1}^{k} x_i\right)^p \geq 0 \tag{C.2}$$

A local minimum in $\mathbb{R}_+^{k+1}$ is characterized by

$$\frac{\partial f(x)}{\partial x_j} = p\left((k+1)^{p-1} x_j^{p-1} - \left(\sum_{i=1}^{k+1} x_i\right)^{p-1}\right) = 0, \qquad j = 1, 2, \ldots, k+1$$

which implies

$$(k+1)x_j = \sum_{i=1}^{k+1} x_i, \qquad j = 1, 2, \ldots, k+1$$

or

$$x_1 = x_2 = x_3 = \ldots = x_{k+1}$$

at which $f(x) = 0$. Moreover, at the boarder of the domain $\mathbb{R}_+^{k+1}$, we have for $p \geq 1$

$$f(x_j = 0) = (k+1)^{p-1} \sum_{\substack{i=1 \\ i \neq j}}^{k+1} x_i^p - \left(\sum_{\substack{i=1 \\ i \neq j}}^{k+1} x_i\right)^p, \qquad j = 1, 2, \ldots, k+1$$

which due to the induction assumption, (C.2), is guarantied to satisfy

$$f(x_j = 0) \geq 0, \qquad j = 1, 2, \ldots, k+1$$

since $(k+1)^{p-1} > k^{p-1}$. The function $f(x) \geq 0$ everywhere in $\mathbb{R}_+^{k+1}$, and the inequality (C.1) is proved.

C.2 Inequality 2

A second inequality is also used. Let $x, y, a \geq 0$, $m = 1, 2, 3, \ldots$, and define

$$\begin{aligned} & y^2 + \frac{x^2}{a+m} - \frac{(x+y)^2}{a+m+1} \\ &= \frac{y^2(a+m)(a+m+1) + x^2(a+m+1) - (x^2+y^2+2xy)(a+m)}{(a+m)(a+m+1)} \\ &= \frac{y^2(a+m)^2 + x^2 - 2xy(a+m)}{(a+m)(a+m+1)} = \frac{(y(a+m)-x)^2}{(a+m)(a+m+1)} \geq 0 \end{aligned}$$

Appendix References

[1] E. Berrocal et al. "Application of structured illumination for multiple scattering suppression in planar laser imaging of dense sprays". *Optics Express* 16.22 (2008), pp. 17870–17881.

[2] M. J. Dyer and D. R. Crosley. "Two-dimensional imaging of oh laser-induced fluorescence in a flame". *Optics Letters* 7.8 (1982), pp. 382–384.

[3] R. Neil M.A.A. Juskaitis and T. Wilson. "Method of obtaining optical sectioning by using structured light in a conventional microscope". *Optics Letters* 22.24 (1997), pp. 1905–1907.

[4] P. J. Keller and E. H. Stelzer. "Quantitative in vivo imaging of entire embryos with digital scanned laser light sheet fluorescence microscopy". *Current Opinion in Neurobiology* 18 (2008), pp. 624–632.

[5] R. Adrian. "Twenty years of particle image velocimetry". *Experiments in Fluids* 39 (2005), pp. 159–169.

[6] E. Kristensson et al. "High-speed structured planar laser illumination for contrast improvement of two-phase flow images". *Optics Letters* 33.23 (2008), pp. 2752–2754.

[7] E. Kristensson et al. "Analysis of multiple scattering suppression using structured laser illumination planar imaging in scattering and fluorescing media". *Optics Express* 19.14 (2011), pp. 13647–13663.

[8] P. Bouguer. *Essai d'optique*. 1729.

[9] M. I. Mishchenko. *Electromagnetic Scattering by Particles and Particle Groups*. Cambridge University Press, 2014.

[10] X. Ma et al. "Determination of complex refractive index of polystyrene microspheres from 370 to 1610 nm". *Physics in medicine and biology* 48.24 (2003), p. 4165.

[11] S. Chandrasekhar. *Radiative Transfer*. Dover Publications, 1960.

[12] A. Ishimaru. *Wave propagation and scattering in random media. Volume 1. Single scattering and transport theory*. Academic Press, 1978.

[13] M. I. Mishchenko, L. D. Travis, and A. A. Lacis. *Multiple scattering of light by particles: radiative transfer and coherent backscattering*. Cambridge University Press, 2006.

[14] R. L.-T. Cheung and A. Ishimaru. "Transmission, backscattering, and depolarization of waves in randomly distributed spherical particles". *Applied Optics* 21.20 (1982), pp. 3792–3798.

[15] A. Ishimaru. "Theory and application of wave propagation and scattering in random media". *Proc. IEEE* 65.7 (1977), pp. 1030–1061.

[16] A. Deepak, U. O. Farrukh, and A. Zardecki. "Significance of higher-order multiple scattering for laser beam propagation through hazes, fogs, and clouds". *Applied optics* 21.3 (1982), pp. 439–447.

[17] W. Tam and A. Zardecki. "Multiple scattering of a laser beam by radiational and advective fogs". *Optica Acta: International Journal of Optics* 26.5 (1979), pp. 659–670.

[18] R. Fante. "Propagation of electromagnetic waves through turbulent plasma using transport theory". *IEEE Trans. Antennas Propag.* 21.5 (1973), pp. 750–755.

[19] M. Linne et al. "Ballistic imaging of liquid breakup processes in dense sprays". *Proc Comb Inst* 32 (2009), pp. 2147–2161.

[20] G. Wentzel. "Zur Theorie der Streuung von ß-Strahlen". *Annalen der Physik* 374.21 (1922), pp. 335–368.

[21] W. T. Scott. "The theory of small-angle multiple scattering of fast charged particles". *Rev. Mod. Phys.* 35.2 (1963), p. 231.

[22] I. S. Gradshteyn and I. M. Ryzhik. *Table of Integrals, Series, and Products*. Seventh. Academic Press, 2007.